NeuroImage 259 (2022) 119396

Contents lists available at ScienceDirect

NeuroImage

journal homepage: www.elsevier.com/locate/neuroimage

Impact of spill-in counts from off-target regions on [^{18}F]Flortaucipir PET quantification

Francisco J. López-González[a,b,1], Alejandro Costoya-Sánchez[a,c,1], José Paredes-Pacheco[a,b], Alexis Moscoso[d], Jesús Silva-Rodríguez[c,e,*], Pablo Aguiar[a,c], for the Alzheimer's Disease Neuroimaging Initiative[2]

[a] Molecular Imaging Group, Department of Radiology, Faculty of Medicine and Center for Research in Molecular Medicine and Chronic Diseases (CIMUS), University of Santiago de Compostela (USC), Campus Vida, Santiago de Compostela, Galicia, Spain
[b] Molecular Imaging Unit (UIM), Centro de Investigaciones Médico-Sanitarias (CIMES), General Foundation of the University of Málaga (Fguma), Málaga, Spain
[c] Nuclear Medicine Department and Molecular Imaging Group, University Hospital CHUS-IDIS, Travesía da Choupana s/n, Santiago de Compostela, 15706, Spain
[d] Department of Psychiatry and Neurochemistry, Institute of Neuroscience and Physiology, The Sahlgrenska Academy, and The Wallenberg Centre for Molecular and Translational Medicine, University of Gothenburg, Gothenburg, Sweden
[e] Movement Disorders Unit, Clinical Neurology and Neurophysiology Department, Institute of Biomedicine of Seville, Virgen del Rocío University Hospital/CSIC/University of Seville, Seville, Spain

ARTICLE INFO

Keywords:
Tau PET
Monte Carlo
Off-target binding
PVE
SUVR

ABSTRACT

Background: [^{18}F]Flortaucipir (FTP) PET quantification is usually hindered by spill-in counts from off-target binding (OFF) regions. The present work aims to provide an in-depth analysis of the impact of OFF in FTP PET quantification, as well as to identify optimal partial volume correction (PVC) strategies to minimize this problem.
Methods: 309 amyloid-beta (Aβ) negative cognitively normal subjects were included in the study. Additionally, 510 realistic FTP images with different levels of OFF were generated using Monte Carlo simulation (MC). Images were corrected for PVC using both a simple two-compartment and a multi-region method including OFF regions. FTP standardized uptake value ratio (SUVR) was quantified in Braak Areas (BA), the hippocampus (which was not included in Braak I/II) and different OFF regions (caudate, putamen, pallidum, thalamus, choroid plexus (ChPlex), cerebellar white matter (cerebWM), hemispheric white matter (hemisWM) and cerebrospinal fluid (CSF)) using the lower portion of the cerebellum as a reference region. The correlations between OFF and cortical SUVRs were studied both in real and in simulated PET images, with and without PVC.
Results: In-vivo, we found correlations between all OFF and target regions, especially strong for the hemisWM (slope>0.63, R^2>0.4). All the correlations were attenuated but remained significant after applying PVC, except for the ChPlex. In MC simulations, the hemisWM and CSF were the main contributors to PVE in all BA (slopes 0.15-0.26 and 0.13-0.21 respectively). The hemisWM (slope=0.2), as well as the ChPlex (slope=0.02), influenced

List of abbreviations: PET, Positron Emission Tomography; AD, Alzheimer's disease; Aβ, amyloid beta; NFTs, neurofibrillary tangles; FTP, [^{18}F]Flortaucipir; HC, Healthy Controls; SUVR, Standardized Uptake Value Ratio; BA, Braak Areas; ROI, Region of Interest; PVE, Partial Volume Effect; OFF, Off-target binding; $HC_{A\beta-}$, Aβ-negative healthy controls; PVC, Partial Volume Correction; ADNI, Alzheimer's Disease Neuroimaging Initiative; HABS, Harvard Aging Brain Study; MC, Monte Carlo; MRI, Magnetic Resonance Imaging; MCI, Mild Cognitive Impairment; SPM, Statistical Parametric Mapping; RBV, Region-Based Voxel-wise; GTM, Geometric Transfer Matrix; WM, White matter; GM, Grey matter; ChPlex, Choroid Plexus; hemisWM, hemispheric White Matter; cerebWM, cerebellar White Matter; CSF, Cerebrospinal fluid; SimSET, Simulation System for Emission Tomography; OS-EM, Ordered Subsets Expectation Maximization algorithm; STIR, Software for Tomographic Image Reconstruction; MNI, Montreal Neurological Institute.

* **Corresponding author**: Jesús Silva-Rodríguez, Unidad de Trastornos del Movimiento, Instituto de Biomedicina de Sevilla, Hospital Universitario Virgen del Rocío, Avda. Manuel Siurot s/n, 41013, Seville, Spain
E-mail address: jsilva-ibis@us.es (J. Silva-Rodríguez).

[1] FJLG and ACS equally contributed to this work and share the first authorship.

[2] Data used in the preparation of this article were obtained from the Alzheimer's Disease Neuroimaging Initiative (ADNI) database (adni.loni.usc.edu). As such, the investigators within the ADNI contributed to the design and implementation of ADNI and/or provided data but did not participate in the analysis or the writing of this report. A complete listing of ADNI investigators can be found at: http://adni.loni.usc.edu/wpcontent/uploads/how_to_apply/ADNI_Acknowledgement_List.pdf

https://doi.org/10.1016/j.neuroimage.2022.119396.
Received 7 February 2022; Received in revised form 23 May 2022; Accepted 15 June 2022
Available online 24 June 2022.

SUVRs in the hippocampus. The CerebWM was negatively correlated with all target regions (slope<-0.02, R^2>0.8). While no other correlations between OFF and target regions were found, hemisWM was correlated with all OFF regions but the cerebWM (slopes 0.06-0.33). HemisWM correlations attenuated (slopes<0.06) when applying two-compartment PVC, but the hippocampus-ChPlex and the cerebWM correlations required more complex PVC with dedicated compartments for these regions. In-vivo, PVC removed a notably higher fraction of the correlation between OFF regions found to be affected by PVE in the simulation studies and BA (≈50%) than for OFF regions not affected by PVE (16%).

Conclusion: HemisWM is the main driver of spill-in effects in FTP PET, affecting both target regions and the rest of OFF regions. PVC successfully reduces PVE, even when using a simple two-compartment method. Despite PVC, non-zero correlations were still observed between target and OFF regions in vivo, which suggests the existence of biological or tracer-related contributions to these correlations.

1. Background

In recent years, Positron Emission Tomography (PET) has become a reference tool for the diagnosis and monitoring of Alzheimer's disease (AD), mainly due to the emergence of radiotracers targeting extracellular amyloid-beta (Aβ) plaques and intraneuronal tau neurofibrillary tangles (NFTs) (Schöll et al., 2016; Schultz et al., 2018). Specifically, [^{18}F]Flortaucipir (FTP, also referred to as [^{18}F]T807 or [^{18}F]AV-1451) has been adopted for detecting pathological tau accumulation in AD patients (Chien et al., 2013; Leuzy et al., 2019) due to its high affinity for 3R/4R tau isoforms characteristic of AD (Xia et al., 2013). FTP has shown high sensitivity and specificity in discriminating AD patients from healthy controls (HC) and in monitoring disease progression (Johnson et al., 2016; Maass et al., 2017; Ossenkoppele et al., 2018; Schöll et al., 2016; Schrouff et al., 2013; Schwarz et al., 2016; Wang et al., 2016). Furthermore, FTP PET staging schemes were found to match those previously established in post-mortem studies (Braak and Braak, 1991; Chen et al., 2021; Schwarz et al., 2018). PET staging methods are typically based on the quantification of standardized uptake value ratios (SUVR) in Braak Areas (BA ROIs) (Chen et al., 2021) and have been proven successful for in-vivo staging of AD patients (Schöll et al., 2016).

Nevertheless, FTP PET quantification still poses challenges related to PET imaging noise and limited resolution, which cause variability and partial volume effects (PVE), respectively. Due to the limited resolution of PET scanners (typically in the range of 3-6 mm), the detected counts are commonly spread across adjacent regions (Aston et al., 2002). These exchanges of counts caused by PVE are also referred to as spill-out (or -in) effects (Lu et al., 2021). Despite FTP having shown high specificity for AD tau pathology, several brain areas have also been reported to exhibit unspecific off-target binding (OFF), such as the white matter, basal ganglia, choroid plexus or blood vessels, among others (Chandra et al., 2019; Lowe et al., 2016). Due to PVE, counts from these OFF regions can spread into cortical ROIs and alter SUVR measurements (Hoffman et al., 1979). These effects become more severe as AD progresses due to cortical atrophy (Gonzalez-Escamilla et al., 2017). In a previous work (Baker et al., 2019), the authors investigated the relationship between OFF and cortical binding in 90 Aβ-negative healthy controls ($HC_{A\beta-}$), reporting that cortical SUVR measurements are heavily influenced by OFF. Furthermore, the authors applied a novel PVE correction (PVC) technique to correct for PVE of the most relevant OFF regions in FTP and reported that PVC cannot remove all the OFF-BA signal correlation. These remaining correlations may be explained by several factors such as the presence of biological or tracer-related correlations between uptake in different OFF regions and disease progression (Moscoso et al., 2021), or by technical factors such as PVC not being able to correct for all PVE. Nevertheless, discerning between technical and biological contributions to this correlation is inherently challenging, and further investigation on the effects of OFF may play a vital role in determining the clinical utility of FTP (Roy et al., 2021).

In the present work we perform a systematic study of the contribution of spill-in counts from OFF regions to FTP PET SUVR quantification, isolating technical from biological or tracer-related effects. To achieve this, we analysed FTP PET data from a large sample of 309 $HC_{A\beta-}$ subjects from the Alzheimer's Disease Neuroimaging Initiative (ADNI, adni.loni.usc.edu) and the Harvard Aging Brain Study (HABS, habs.mgh.harvard.edu) together with a large set of synthetic images generated using a well-controlled Monte Carlo (MC) simulation framework (Paredes-Pacheco et al., 2021). This strategy allowed for the generation of realistic FTP PET images derived from real patient data that included different levels of spill-in counts from OFF regions, providing an estimation of the magnitude of purely technical contributions to PVE.

2. Methods

2.1. Subject data

Data used in the preparation of this article were obtained from the ADNI and HABS databases. The ADNI was launched in 2003 as a public-private partnership, led by Principal Investigator Michael W. Weiner, MD. The primary goal of ADNI has been to test whether serial magnetic resonance imaging (MRI), PET, other biological markers, and clinical and neuropsychological assessment can be combined to measure the progression of mild cognitive impairment (MCI) and early AD. HABS was started in 2010, funded by the National Institute of Aging and led by Principal Investigators Reisa A. Sperling, MD and Keith A. Johnson, MD.

Our cohort includes 309 $HC_{A\beta-}$ subjects from ADNI and HABS who underwent structural MRI, Aβ PET and FTP PET scans, with Aβ negativity defined as centiloid 12 or lower (Klunk et al., 2015). Demographic characteristics of the joint cohort are detailed in Supplementary Table 1. In addition, a subset of ten randomly selected ADNI subjects acquired with the GE Discovery ST (6 males and 4 females; mean age: 78.98 ± 6.42 yrs. range: 71.5-89.4 yrs) was used as input for the MC simulation framework following the methodology described below (detailed information about these subjects is provided in Supplementary Table 2).

2.2. Image Acquisition

ADNI FTP PET images were acquired using dynamic 3D acquisitions of six 5-min frames starting 75 minutes after the injection of 370 MBq ± 10% of FTP. Every image was reviewed for protocol compliance by the ADNI PET Quality Control team. For this work, we used images in pre-processing levels two and four as described by ADNI (http://adni.loni.usc.edu/methods/pet-analysis-method/pet-analysis/), which corresponds to co-registered and averaged images (level two), further reoriented to a standard image matrix and smoothed to 8 mm isotropic resolution (level four). Level four is used throughout this study unless stated otherwise.

HABS FTP PET images were acquired using dynamic 3D acquisitions after the injection of 370 MBq ± 10% of FTP. Acquisition varies between four 5-min frames starting at 80 min post-injection and six 5-min frames starting at 75 min post-injection. Static PET images were then obtained by realigning and averaging the acquired frames and reslicing the images to the ADNI standard voxel size of 1.5 mm. Afterwards, an isotropic Gaussian filter of FWHM 5 mm was applied to harmonize the images to the ADNI standard resolution of 8 mm.

T1 structural scans from ADNI and HABS were acquired on 3T scanners using an accelerated sagittal MPRAGE sequence with a spatial resolution of 1 cubic millimeter (mm^3). Each series in each exam underwent quality control following the steps described in detail in ADNI's MRI protocol (http://adni.loni.usc.edu/methods/mri-tool/mri-analysis/).

2.3. Image processing

FTP PET images were co-registered to the corresponding MRI using the standard multi-modal volume registration (Wells et al., 1996) and processed using the code shared by Baker et al. (Baker et al., 2017). This code takes as inputs the co-registered tau PET and MRI images, and the segmentations from both FreeSurfer (FreeSurfer version 6, http://surfer.nmr.mgh.harvard.edu/) and SPM (Statistical Parametric Mapping version 12, http://www.fil.ion.ucl.ac.uk/spm/). The output of the code is a subject-specific atlas including cortical and OFF ROIs relevant for FTP PET quantification. Following the recommendations from the authors, we used ROI configuration number 8 in the method publication for generating the subject atlases (Baker et al., 2017). The results of the SPM segmentation were also used to transform the SUIT cerebellar template (Diedrichsen et al., 2009) to each subject's space to obtain the inferior cerebellum grey matter ROI to be used as a reference region for SUVR quantification. Then, FTP PET images were corrected for PVE using the open-source PETPVC toolbox (Thomas et al., 2016) with the region-based voxel-wise correction (RBV) method, an extension of the popular Rousset Geometric Transfer Matrix method (GTM) (Rousset et al., 1998) and the voxel-wise correction by Yang et al. (Yang et al., 1996). For smoothed data, a point spread function (PSF) of 8 mm x 8 mm x 8 mm was used for PVC, while the PSF values as measured by the NEMA-NU 2-2012 standards (Nema, 2012) were used for unsmoothed data. Two different atlases were used for PVC. First, the subject-specific atlas generated with Baker's code (Baker et al., 2017); second, a simplified atlas including ROIs only for the subject's white matter (WM) and grey matter (GM). This later atlas was obtained by combining the GM and WM regions from the Baker's atlas.

Freesurfer segmentation ROIs from the Desikan atlas were combined to generate Braak I/II, Braak III/IV, and Braak V/VI areas (Biel et al., 2021). The hippocampus was not included in Braak I/II, following recommendations from previous studies (Maass et al., 2017), but it was included as a separate ROI as it might be of interest for the interpretation of other studies. Detailed information on the ROIs included on each BA can be found in Supplementary Table 3. The caudate, putamen, pallidum, thalamus, choroid plexus (ChPlex), hemispheric white matter (hemisWM), cerebellar white matter (cerebWM) and cerebrospinal fluid (CSF) were included as OFF regions (Baker et al., 2019). Fig. 1 shows BA, hippocampus, and OFF regions for one of the subjects.

2.4. In-vivo FTP PET quantification

Regional SUVRs were calculated for the target ROIs (BA and hippocampus) and for the OFF regions from both non-PVC and PVC images. Analyses are detailed in the *Statistical Analysis* section. Additionally, the average uptake and variability of each of the OFF ROIs was characterized as the (mean ± 2 SDs) interval and was used for configuring OFF ROI values in the activity maps for the simulation experiments (see *Monte Carlo simulation* section).

2.5. Monte Carlo simulation

2.5.1. Generation of the activity and attenuation maps

From the previously described cohort of $HC_{A\beta-}$ subjects, 10 subjects acquired using a GE Discovery ST scanner (ADNI IDs 4100, 4292, 4376, 6333, 6575, 6580, 0734, 4179, 6298, 6352) were used to generate realistic subject-specific activity and attenuation maps. The map generation process is explained in detail elsewhere (Marti-Fuster et al., 2014; Paredes-Pacheco et al., 2021). In brief, the subject-specific atlas and the co-registered PET image (level 2 of ADNI processing) were used to create preliminary activity and attenuation maps, which are then simulated and reconstructed using the validated MC model of the GE Discovery ST incorporated in the SimPET platform (Paredes-Pacheco et al., 2021). After the reconstruction, the activity map is updated based on a voxel-wise comparison between the simulated and acquired images. In an iterative-reconstruction fashion, the process is repeated until the correlation coefficient between the simulated and the subject PET images is ≥0.99. Fig. 2 shows a schematic representation of the process.

Once each subject's activity map was generated, the maps were modified to generate different uptake levels in the 8 OFF ROIs listed above. First, OFF binding was minimized by fixing a SUVR of 0.5 (this condition was considered as no-OFF binding). Then, 5 different SUVR values were generated within the (mean ± 2 SDs) range for each OFF ROI. This range of SUVR values for the different OFF ROIs was measured from our patient cohort after applying Baker's RBV. Supplementary Table 4 details the five simulated SUVR values for each of the OFF ROIs. In addition to varying the values of each OFF ROI individually, several groups of ROIs that were found to vary together on our in-vivo analysis were also considered and simulated co-varying together. Namely, these clusters were: i) caudate, putamen and pallidum and ii) thalamus, hemisWM and cerebWM. This resulted in a total of 510 FTP simulated images with their corresponding ground-truths (activity maps).

2.5.2. MC simulation and tomographic reconstruction

The MC model of the GE Discovery ST scanner included on the SimPET platform was used for the simulation of the 510 generated activity maps together with their corresponding attenuation maps. The simulation was performed with SimSET v2.9.2 (Simulation system for emission tomography) (Haynor et al., 1991), with times fixed to replicate the 30 min total acquisition times in the subject PET studies.

The tomographic reconstruction was performed using the ordered subsets expectation maximization algorithm (OS-EM) (Hudson and Larkin, 1994) as implemented in STIR 4.1.1 (Software for tomographic image reconstruction) (Thielemans et al., 2012) including 7 subsets and 5 iterations. Neither post-filtering nor inter-iteration filtering was applied. The matrix and voxel size of the reconstructed images were 128 × 128 × 47 and 1.95 mm x 1.95 mm x 3.27 mm, respectively.

2.6. Simulated FTP PET quantification

All the simulated images were quantified following the quantification pipelines used for real subjects, including the application of the different PVCs. Regional SUVR values were obtained for the target (BA and hippocampus) and for the OFF regions. To replicate the analysis performed in the in-vivo cohort, complementary analysis was performed after smoothing the images from the MC model (resolution of 4.9 mm (x), 4.8 mm (y) and 7.9 mm (z)) to an isotropic resolution of 8 mm.

2.7. Statistical analysis

Correlation analysis was performed using linear regression models of the form $A = \beta_0 + \beta_1 B$ (where *A (target ROI SUVR) and B (OFF ROI SUVR)* are the pair of studied variables, and β_0, β_1 are the intercept and slope of the regression, respectively). When several regions were co-varied together, the regression took the form of $A = \beta_0 + \beta_1 B_1 + \beta_2 B_2 + \ldots + \beta_i B_i$ where β_1, β_2,..., β_i are the coefficients (slopes) for each OFF region.

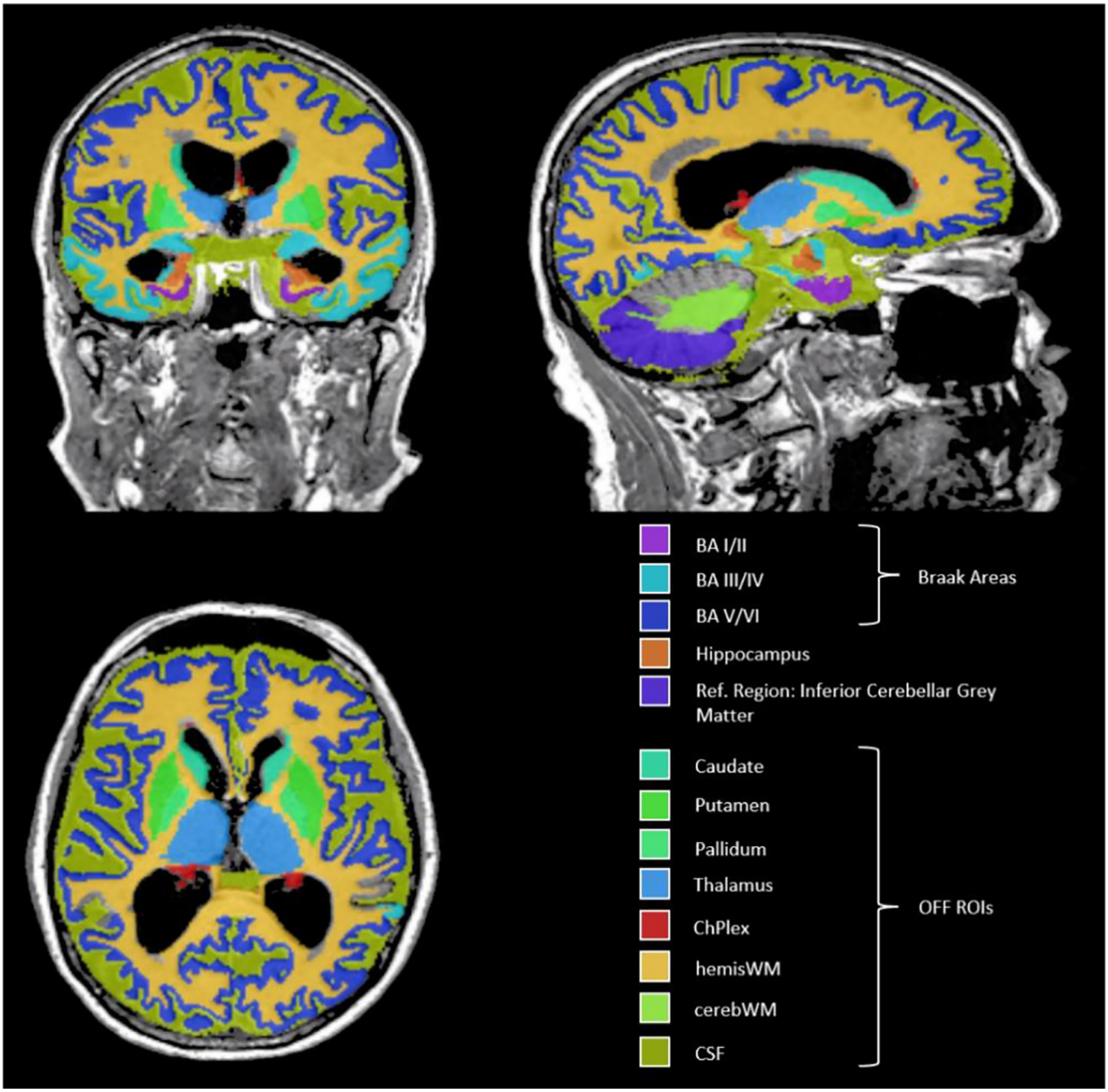

Fig. 1. Braak Areas (BA), hippocampus and Off-target binding (OFF) regions of interest (ROIs) for one of the study participants.

Correlation effects were studied by using both using coefficient of determination (R^2) and the βs (slopes). In a regression model, R^2 determines the proportion of variance in the dependent variable (i.e., target SUVR) that can be explained by the independent variable (i.e., OFF ROI SUVR) and it is defined as $1\text{-}SS_{res}/SS_{tot}$; SS_{res} is the sum of squares of residuals (how well the regression model represents the data) and SS_{tot} is the total sum of squares (the whole variance in the data). Results were considered significant when the p-value for the β_1 parameter was lower than 0.05.

We present analyses of the correlations between SUVRs on the target (BA and hippocampus) and OFF regions for both non-PVC and PVC images, both in vivo and simulated images. Additionally, pair-wise correlations between in vivo OFF regions, as well as correlations of each OFF ROI and age (Barret et al., 2017) were studied. Similarly, PVE-related correlations between individual pairs of OFF ROIs were investigated on the simulated images.

3. Results

3.1. Comparison between no-OFF and PVC on simulated images

Fig. 3 (left) shows examples of the simulated activity maps. Fig. 3 (right) shows a visual comparison between real, simulated and no-OFF simulated images for non-PVC, Baker's RBV and GM/WM (from top to bottom). Fig. 4 shows the comparison between SUVR measurements of these groups, including also the simulated SUVR (activity map) as a reference. The average differences across all ROIs in SUVR between real and simulated images were of 0.94% (non-PVC, $p>0.5$), 2.23% (Baker's

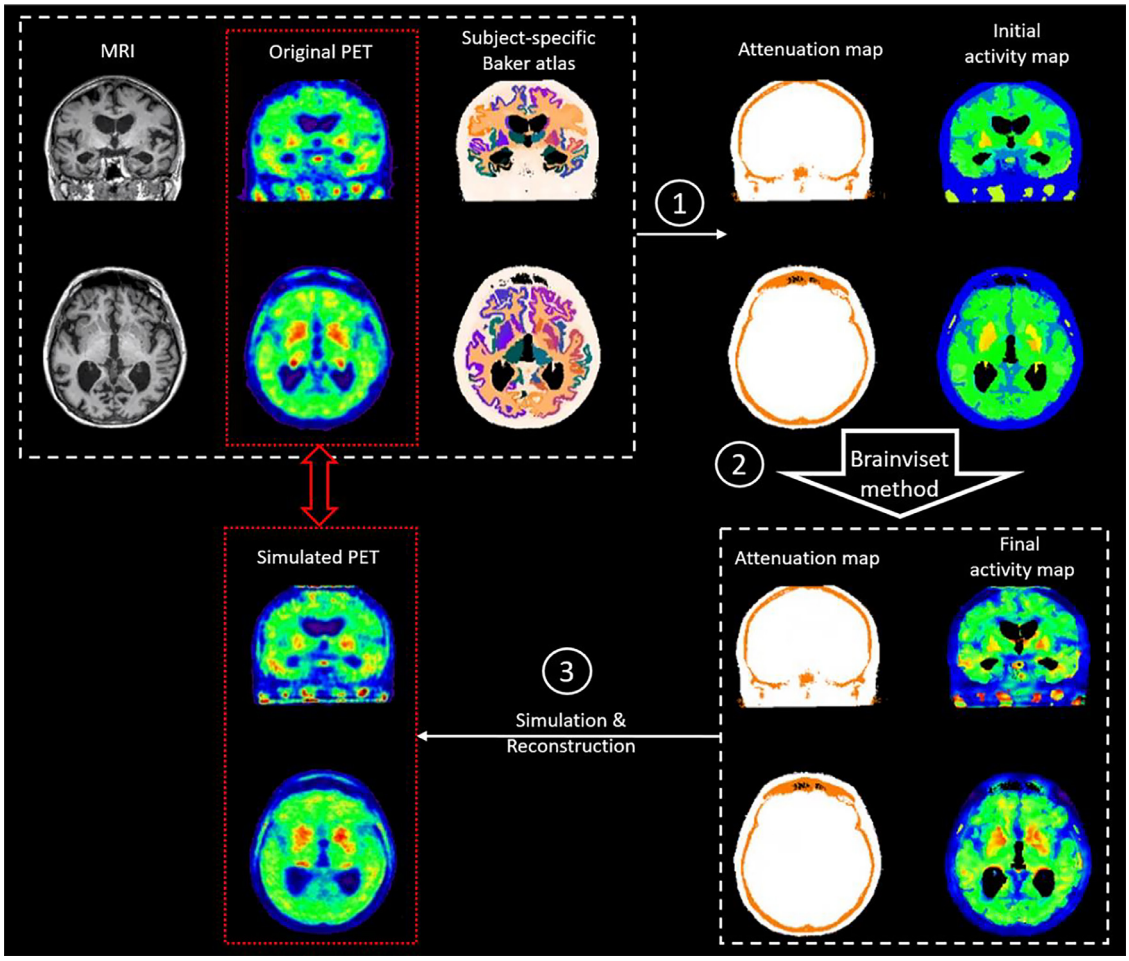

Fig. 2. Schematic representation of the activity and attenuation map's generation. *Step1:* Generation of preliminary activity and attenuation maps. *Step 2:* Brainviset process to obtain realistic subject-specific activity and attenuation maps. *Step 3:* Final simulation and reconstruction.

RBV, p>0.5) and 1.31% (GM/WM RBV, p>0.5), reflecting the good agreement between the simulated and real data. After removing OFF contributions from the simulation (no-OFF), we observed the expected reduction of the measured SUVR without PVC (average = -16.19%, p<0.001). These differences were significantly reduced after applying Baker's RBV (average = -1.73%, p>0.5) but remained after applying the GM/WM RBV (average = -10.04%, p<0.001). We also observed that the measured SUVRs were significantly higher than the simulated SUVRs when applying the GM/WM RBV (p<0.001), an effect that we did not observe for the Baker's RBV or for non-PVC images (p>0.1).

3.2. ADNI and HABS FTP PET analysis

3.2.1. Correlation between target and OFF ROIs

Fig. 5 shows the correlations between SUVRs on the target and OFF regions in the in-vivo cohort. For non-PVC images, linear regression models showed a statistically significant positive relation for all cases. HemisWM showed the highest correlation with all target regions (BA I/II R^2=0.40, slope=0.64; BA III/IV R^2=0.74, slope=0.68; BA V/VI R^2=0.72, slope=0.63; hippocampus R^2=0.47, slope=1.07). For PVC SUVR values, a significant reduction of the hemisWM spill-in effect was observed, mainly after Baker's RBV (BA I/II R^2=0.08, slope=0.36; BA III/IV R^2= 0.26, slope=0.41; BA V/VI R^2=0.10, slope=0.25; hippocampus R^2=0.21, slope=0.79), but also after GM/WM RBV (BA I/II R^2= 0.19, slope=0.49; BA III/IV R^2= 0.28, slope=0.38; BA V/VI R^2= 0.18, slope=0.32; hippocampus R^2=0.34, slope=0.72). A similar pattern was observed for the rest of OFF regions, with statistically significant positive correlations before PVC and decreased R^2 after PVC (linear models in Supplementary Fig. 1). Nevertheless, the reduction on R^2 observed in Fig. 5 was not accompanied by a reduction of the slope for some of the OFF regions (caudate, putamen, pallidum and thalamus) (linear models in Supplementary Fig. 2). Some OFF regions such as the thalamus and ChPlex still showed high spill-in effects on the hippocampus after GM/WM RBV. CSF showed almost no effect on any target ROI, except for BA V/VI without PVC. Finally, to better understand the differences between single- and multi-centric studies, we studied these correlations separately for ADNI (52 sites) and HABS (1 site). No observable differences were found between the results of the two cohorts (Supplementary Fig. 3).

3.2.2. Interactions between OFF regions

Table 1 shows the correlations between OFF ROIs in-vivo. Caudate, putamen and pallidum showed the strongest correlations among themselves before PVC (R^2 0.58-0.90) with subtle or no decrease after Baker's RBV (R^2 0.46-0.64) and GM/WM RBV correction (R^2 0.67-0.86). HemisWM also had a significant correlation between these regions before PVC (R^2 0.52-0.55), which was largely weakened after PVC, especially with Baker's RBV (R^2 0.18-0.33). Thalamus, hemisWM and cerebWM conformed the second group of highly intercorrelated regions before PVC (R^2 0.53-0.64), with virtually no decrease after Baker's (R^2 0.48-0.67) or GM/WM RBV (R^2 0.47-0.82). Lastly, the ChPlex and CSF regions were not correlated with other OFF regions (ChPlex R^2<0.09, CSF R^2<0.06), except for the ChPlex and the thalamus before PVC (R^2=0.34) and after GM/WM RBV (R^2=0.27). Additionally,

Table 1
R^2 values for each pair of OFF regions and age, before PVC, after Baker's RBV, and after GM/WM RBV. *p<0.05. **p<0.0001. Highly correlated ROIs are highlighted in bold.

	Putamen	*Pallidum*	*Thalamus*	*ChPlex*	*CerebWM*	*HemisWM*	*CSF*	*Age*
Caudate								
No PVC	***0.61*****	***0.58*****	*0.50***	*0.09***	*0.39***	*0.52***	*0.00*	*0.03**
Baker's RBV	***0.64*****	***0.46*****	*0.35***	*0.04**	*0.22***	*0.22***	*0.01*	*0.06***
GM/WM RBV	***0.77*****	***0.67*****	*0.49***	*0.06**	*0.27***	*0.38***	*0.01*	*0.10***
Putamen								
No PVC		***0.90*****	*0.53***	*0.04**	*0.40***	*0.54***	*0.02**	*0.20***
Baker's RBV		***0.53*****	*0.34***	*0.00*	*0.14***	*0.18***	*0.04**	*0.21***
GM/WM RBV		***0.86*****	*0.53***	*0.04**	*0.30***	*0.44***	*0.03**	*0.20***
Pallidum								
No PVC			*0.55***	*0.05***	*0.45***	*0.55***	*0.01**	*0.15***
Baker's RBV			*0.42***	*0.01*	*0.33***	*0.33***	*0.02**	*0.08***
GM/WM RBV			*0.55***	*0.04**	*0.38***	*0.49***	*0.02**	*0.14***
Thalamus								
No PVC				*0.34***	***0.52*****	***0.64*****	*0.00*	*0.04***
Baker's RBV				*0.06**	***0.48*****	***0.52*****	*0.00*	*0.02***
GM/WM RBV				*0.27***	***0.47*****	***0.57*****	*0.01**	*0.07***
ChPlex								
No PVC					*0.04**	*0.06**	*0.00*	*0.02**
Baker's RBV					*0.02**	*0.01*	*0.01*	*0.00*
GM/WM RBV					*0.01*	*0.02**	*0.01**	*0.06***
CerebWM								
No PVC						***0.62*****	*0.00*	*0.00*
Baker's RBV						***0.67*****	*0.01*	*0.03**
GM/WM RBV						***0.82*****	*0.02**	*0.00*
HemisWM								
No PVC							*0.04**	*0.02**
Baker's RBV							*0.06***	*0.00*
GM/WM RBV							*0.01*	*0.02**
CSF								
No PVC								*0.03**
Baker's RBV								*0.03**
GM/WM RBV								*0.02**

age also showed little to no correlation with any OFF region (R^2<0.09), with the exceptions of the putamen (R^2 0.20-0.21) and the pallidum (R^2 0.14-0.15; R^2 <0.08 after Baker's RBV). As in the previous section, in Supplementary Tables 5 and 6 we report the results for the ADNI and HABS cohorts separately. In brief, no significant differences were found between cohorts, with the only exception of a significantly higher correlation between the thalamus and the ChPlex in HABS after Baker's RBV.

3.3. Simulated cohort

From our in-vivo cohort we obtained SUVR ranges (mean ± 2 SDs) of the different OFF ROIs used for the generation of the activity maps for the MC simulation. Specifically: [0.98, 1.49] for the hemisWM, [1.04, 2.03] for the caudate, [1.14, 2.19] for the putamen, [1.23, 2.44] for the pallidum, [1.09, 1.67] for the thalamus, [0.85, 7.25] for the ChPlex, [0.98, 1.43] for the cerebWM and [0.34, 0.91] for the CSF. These values were obtained after Baker's RBV correction, ensuring correct measurements in small areas such as the ChPlex.

On the simulated images, our linear regression models for non-PVC revealed a positive correlation (p<0.05) between target SUVR and simulated hemisWM SUVR for all target regions (BA and hippocampus), with slopes ranging between 0.15 and 0.26. A positive correlation (p<0.05) between the BA SUVRs and the simulated CSF SUVR was also observed (slopes 0.13-0.21). Furthermore, a positive correlation between the hippocampus SUVR and simulated ChPlex SUVR was confirmed with a slope of 0.02 (p<0.001) (the linear regressions for these correlations are shown in Supplementary Fig. 4). For the cerebWM, a negative correlation with all the target regions were observed (p<0.05), with slopes ranging between -0.06 and -0.03. For the rest of the OFF regions (caudate, pallidum, putamen and thalamus) our simulation results did not reproduce the correlations observed in real data (slope<0.02, p>0.05). All the correlations found on non-PVC data severely decreased after applying Baker's RBV (|slope|<0.05). As expected, applying the GM/WM's atlas PVC only reduced the correlations between hemisWM and target regions (BA and hippocampus) (slope<0.05). The correlation between cerebWM and all target regions slightly increased after the GM/WM PVC (maximum slopes from -0.06 to -0.08). For images smoothed to an isotropic resolution of 8 mm, we obtained similar results, with minor variations (increases) in the slopes after smoothing (see Supplementary Table 7).

Furthermore, our in-vivo analysis revealed that some clusters of OFF ROIs co-varied without any notable reduction in correlation after applying PVC. These groups of ROIs were i) caudate, putamen and pallidum and ii) thalamus, hemisWM and cerebWM. Following these findings, we performed additional simulations where each of these groups of ROIs was co-varied together. The results were analysed combined with the data from each of the ROIs varying. As can be seen in Table 2, for group i) the effect of varying the ROIs together did not have any notable effect compared to varying the ROIs individually, with virtually no effect on the SUVR. For group ii), the hemisWM is still the dominant contributor to SUVR variations (slopes 0.15-0.24) when all the group is varied together.

3.3.1. Interactions between OFF regions

Table 3 shows the interactions between the SUVR values of the different OFF regions. In contrast with our in-vivo analysis, a single OFF region varies while the rest remain fixed, allowing us to measure cross-region PVE precisely. The strongest correlations were observed between the hemisWM SUVR and the rest of OFF ROIs (except the cerebWM) before PVC (slopes 0.09-0.39, p<0.001). These correlations were largely weakened after Baker's RBV (slopes 0.02-0.05, p<0.05) except for the ChPlex (slope=0.45, p<0.05), and after GM/WM RBV (slopes 0.00 - 0.12, p<0.05) except for the cerebWM, where a new correlation emerged (slope=0.19, p<5e-5). CSF showed negative correlations with the rest of OFF ROIs but the hemisWM (slopes from –0.06 to -0.02,

Table 2
Series of multi-parametric regression with FTP SUVRs in BA and hippocampus as dependent measure and SUVRs in group i (Caudate, putamen and pallidum) and group ii (Thalamus, hemisWM and cerebWM) as independent measures.

	Dependent variable	Group i				Group ii			
		Independent-variable β				Independent-variable β			
		Caudate	Putamen	Pallidum	R^2	Thalamus	HemisWM	CerebWM	R^2
no PVC	**BA I/II**	0.00	0.00	0.00	0.65	0.00	0.15	-0.04	1.00
	BA III/IV	0.00	0.00	0.00	0.74	0.00	0.21	-0.04	1.00
	BA V/VI	0.00	0.00	0.00	0.73	-0.01	0.24	-0.04	1.00
	Hippocampus	0.00	0.00	0.00	0.54	0.00	0.18	-0.04	1.00
Baker's RBV	**BA I/II**	0.00	0.00	0.00	0.27	0.01	0.04	0.03	0.92
	BA III/IV	0.00	0.00	0.00	0.61	0.00	0.01	0.02	0.89
	BA V/VI	0.00	-0.01	0.00	0.79	-0.01	0.00	0.02	0.78
	Hippocampus	0.00	0.00	0.00	0.64	-0.01	-0.02	0.01	0.92
GM/WM RBV	**BA I/II**	0.01	0.01	0.01	0.78	0.01	0.07	-0.05	0.99
	BA III/IV	0.00	0.00	0.00	0.88	0.01	0.06	-0.06	0.99
	BA V/VI	0.01	0.00	0.01	0.84	0.01	0.08	-0.05	0.99
	Hippocampus	0.00	0.00	0.00	0.57	0.02	0.04	-0.06	0.99

Table 3
Slopes for the correlations between OFF ROIs before PVC, after Baker's RBV and after GM/WM RBV PVCs. $^{*}p<0.05$. $^{**}p<0.0001$. In bold, ROIs for which |slope|>0.02 for any of the items.

		Fixed ROI							
		Caudate	Putamen	Pallidum	Thalamus	ChPlex	CerebWM	HemisWM	CSF
Varying ROI	***Caudate***								
	No PVC		*0.02**	*0.01*	*0.01*	*0*	*0*	*0.01**	*0*
	Baker's RBV		*0.01**	*0*	*-0.01**	*0.02**	*0*	*0*	*0*
	GM/WM RBV		*0.01**	*0.01*	*0*	*0*	*0*	*0*	*0*
	Putamen								
	No PVC	*0.02**		***0.23****	*0*	*0*	*0*	*0.01**	*0*
	Baker's RBV	*0*		***0***	*0*	*0.01*	*0*	*0*	*0*
	GM/WM RBV	*0.01**		***0.15****	*0*	*0*	*0*	*0*	*0*
	Pallidum								
	No PVC	*0*	***0.09****		*0.01**	*0*	*0*	*0*	*0*
	Baker's RBV	*-0.01*	***-0.01****		*0.01**	*-0.01*	*0*	*0*	*0*
	GM/WM RBV	*0*	***0.06****		*0.01**	*0*	*0*	*0*	*0*
	Thalamus								
	No PVC	*0.01*	*0.01*	***0.04****		***0.15****	*0*	*0*	*0*
	Baker's RBV	*-0.01*	*0*	***0.03****		***-0.10****	*0*	*0*	*0*
	GM/WM RBV	*0.01**	*0.01*	***0.03****		***0.01****	*-0.01**	*-0.01**	*0*
	ChPlex								
	No PVC	*0*	*0*	*0*	*0.02**		*0*	*0*	*0*
	Baker's RBV	*0*	*0*	*0*	*-0.01**		*0*	*0*	*0*
	GM/WM RBV	*0*	*0*	*0*	*0.02**		*0*	*0*	*0*
	CerebWM								
	No PVC	***-0.02****	***-0.04****	***-0.04****	***-0.03****	***-0.03****		***-0.03****	***-0.03****
	Baker's RBV	***0.02***	***0.01***	***0.02***	***0.01***	***0.01***		***0.01***	***0***
	GM/WM RBV	***-0.03****	***-0.05****	***-0.04****	***-0.03****	***-0.01****		***0.01****	***0***
	HemisWM								
	No PVC	***0.32****	***0.39****	***0.34****	***0.17****	***0.32****	***0***		***0.09****
	Baker's RBV	***0.02***	***0.05****	***0.03****	***0.03****	***0.45****	***0.01***		***0.02****
	GM/WM RBV	***0.12****	***0.12****	***0.10****	***0.09****	***0.01****	***0.19****		***0***
	CSF								
	No PVC	***-0.04****	***-0.05****	***-0.06****	*-0.02**	***-0.03****	***-0.03****	***0.03****	
	Baker's RBV	***0***	***0***	***-0.01***	*0.01**	***-0.02***	***0.02****	***0.01****	
	GM/WM RBV	***-0.03****	***-0.03****	***-0.03****	*-0.02**	***0***	***-0.09****	***-0.09****	

p<0.05), and these were weakened only after Baker's RBV (slopes from –0.02 to 0.01, p>0.01). The correlation between CSF and cerebWM increased after GM/WM PVC. The putamen and the pallidum were correlated before PVC (slopes 0.09 and 0.23, p<5e-5) and these correlations disappeared after Baker's RBV but not after GM/WM RBV. The thalamus was correlated with the ChPlex (0.15, p<0.05) and the pallidum (0.04, p<0.05) and these correlations were reduced but still significant after PVC. Finally, a correlation between the cerebWM and all the other OFF ROIs was also observed (slopes from -0.04 to -0.02, p<0.05) before PVC. This correlation significatively decreased after Baker's PVC correction (slopes 0.00 - 0.02, p>0.01) but persisted after GM/WM (slopes from -0.05 to -0.01, p<0.05) except for the hemisWM and the CSF. After smoothing to a resolution of 8 mm, we did not observe notable changes in the interpretation of the results, with some slightly higher slopes, especially for the ChPlex (the slope increased from 0.45 to 0.56 after smoothing) (see Supplementary Table 8).

3.4. In-vivo vs. simulated data

Table 4 shows a comparison between the slopes of each of the reported correlations (BA vs. OFF, non-PVC, Baker's RBV and GM/WM RBV) for both in-vivo and simulated data. In general, slopes were significantly lower in simulated data than in real data, which suggests an additional biological/tracer-related contribution to the total slope.

Table 4
Slopes from the linear fits in the in-vivo and simulated cohorts ($^{+}$p>0.05). *For non-PVC regions with |slope|>0.01, we calculate the % reduction after PVC.

		no PVC		Baker's RBV		GM/WM RBV	
OFF ROI	**Target ROI**	**In-vivo**	**Simulated**	**In-vivo (% change after PVC*)**	**Simulated (% change after PVC*)**	**In-vivo (% change after PVC*)**	**Simulated (% change after PVC*)**
Caudate	BA I/II	0.31	0.01^{+}	0.25 (-19)	0.01	0.37 (+16)	0.01
	BA III/IV	0.31	0.00^{+}	0.21 (-32)	0.01^{+}	0.33 (+9)	0.01^{+}
	BA V/VI	0.28	0.00^{+}	0.20 (-29)	0.00^{+}	0.31 (+11)	0.00^{+}
	Hippocampus	0.5	0.00^{+}	0.22 (-56)	0.00^{+}	0.47 (-6)	0.00^{+}
Putamen	BA I/II	0.26	0.00^{+}	0.27 (+4)	0.00^{+}	0.39 (+50)	0.00^{+}
	BA III/IV	0.26	0.00^{+}	0.22 (-15)	0.00^{+}	0.34 (+31)	0
	BA V/VI	0.21	0.00^{+}	0.17 (-19)	0.00^{+}	0.29 (+38)	0
	Hippocampus	0.44	0.00^{+}	0.33 (-25)	0.01^{+}	0.54 (+23)	0.01^{+}
Pallidum	BA I/II	0.23	0.00^{+}	0.22 (-4)	0.00^{+}	0.33 (+43)	0.00^{+}
	BA III/IV	0.23	0.00^{+}	0.17 (-26)	0.00^{+}	0.27 (+17)	0.00^{+}
	BA V/VI	0.18	0.00^{+}	0.13 (-28)	0	0.22 (+22)	0
	Hippocampus	0.39	0.00^{+}	0.26 (-33)	-0.01^{+}	0.45 (+48)	0.00^{+}
Thalamus	BA I/II	0.41	-0.01^{+}	0.44 (+7)	-0.02^{+}	0.48 (+15)	-0.01^{+}
	BA III/IV	0.4	0.00^{+}	0.45 (+13)	0	0.35 (-13)	0.00^{+}
	BA V/VI	0.34	0.00^{+}	0.35 (+3)	-0.01^{+}	0.30 (+13)	0.00^{+}
	Hippocampus	0.98	0.02	0.96 (-2)	0.02 (0)	0.93 (-5)	0.03 (+50)
hemisWM	BA I/II	0.64	0.15	0.36 (-44)	0.01^{+} (-93)	0.49 (-23)	0.05 (-67)
	BA III/IV	0.68	0.22	0.41 (-40)	0.01^{+} (-95)	0.38 (-44)	0.04 (-82)
	BA V/VI	0.63	0.26	0.25 (-60)	-0.01 (-104)	0.32 (-49)	0.05 (-81)
	Hippocampus	1.07	0.2	0.79 (-26)	-110.02	0.72 (-33)	0.04 (-80)
cerebWM	BA I/II	0.61	-0.03	0.36 (-41)	0.05 (+267)	0.40 (-34)	-0.04 (+33)
	BA III/IV	0.63	-0.04	0.41 (-35)	0.03 (+175)	0.28 (-56)	-0.06 (+50)
	BA V/VI	0.54	-0.03	0.31 (-43)	0.02 (+167)	0.18 (-67)	-0.06 (+100)
	Hippocampus	1.14	-0.06	0.57 (-50)	82.99	0.68 (-40)	-0.08 (+33)
chPlex	BA I/II	0.10^{+}	0	~0.00^{+} (-100)	0.01	0.08 (-20)	0
	BA III/IV	0.06^{+}	0	~0.00^{+} (-100)	0	0.04 (-33)	0
	BA V/VI	0.04	0	0.01 (-75)	0.00^{+}	0.03 (-25)	0.00^{+}
	Hippocampus	0.38	0.02	0.07 (-82)	-0.01 (-150)	0.27 (-29)	0.02 (0)
CSF	BA I/II	0.34	0.19	-0.24 (-170)	0.01^{+} (-95)	0.98 (+188)	0.30 (-58)
	BA III/IV	0.33	0.13	-103.01	0.01^{+} (-92)	0.56 (+70)	0.20 (-54)
	BA V/VI	0.47	0.21	-109.04	-0.02 (-110)	0.75 (+37)	0.34 (-62)
	Hippocampus	0.18^{+}	0.03	0.22 (+22)	0.05 (-67)	-161.11	0.07 (-133)

For the ROIs that were found to contribute to BA and hippocampus SUVR through PVE in the simulated data (hemisWM, CSF, ChPlex and cerebWM), applying Baker's RBV produced and average reduction in the slopes of the linear fits for real data of 0.215±0.149 (-53.7±40.1 %), while applying the GM/WM RBV produced a reduction of 0.205±0.155 (-47.1±22.5 %). For the hemisWM, which was found to contribute the most to PVE both in-vivo and on simulated data, both PVCs performed similar in-vivo, with reductions of -42.5±14.0 % and -37.5±11.6 % for the Baker's RBV and the GM/WM RBV, respectively. Interestingly, for the ROIS where PVE to the target regions was not observed in the simulations (Caudate, putamen, pallidum and thalamus), the average reduction in the slopes was much more modest, with a reduction of 0.06±0.08 (-16.3±18.5 %) after applying Baker's RBV and an increase in the slopes (0.04±0.05, 21.2±18.4 %) after applying GM/WM RBV, as it would be expected if these correlations were driven by factors other than PVE.

4. Discussion

Previous works (Baker et al., 2019; Chandra et al., 2019; Lowe et al., 2016) reported strong correlations between SUVRs measured on OFF and cortical regions that were only partially corrected when applying sophisticated PVC (Baker et al., 2019). While this could be attributed to the PVC not being able to correct all the PVE, the authors also hypothesised that the remaining correlation between OFF and BA signal might be a biological feature of FTP binding properties. This is compatible with previous findings suggesting that the uptake of some of these OFF regions, namely the white matter, might be biologically meaningful and not totally unspecific (Moscoso et al., 2021; Wen et al., 2021). To test these hypotheses, we present an investigation of OFF spill-in contribution to cortical SUVR measurements in a reliable and well-controlled MC simulation environment, combined with an in-depth analysis of these contributions in vivo, adding substantial evidence to previous results (Baker et al., 2019) using an independent and larger dataset.

In our study, we observed positive correlations between the hemisWM and all the target regions (BA and hippocampus) both on simulated (slopes 0.15-0.26, R^2>0.99) and in-vivo data (slopes 0.63-1.07, R^2>0.4). Furthermore, we also observed that the rest of the OFF regions were correlated with the hemisWM (see Table 1, Table 3), indicating a strong impact of PVE from the hemisWM to both OFF and cortical regions. In our simulation experiments we also detected positive correlations between the CSF and the BA (slopes 0.13-0.21, R^2>0.99) but these could not be replicated in-vivo, probably because of the low uptake of the CSF (0.34-0.91) in comparison to other OFF regions such as the hemisWM (0.98-1.49), which might mask PVC from the CSF (Akerele et al., 2018). In addition, a correlation was observed between the ChPlex and the hippocampus, which is in good agreement with previous results (Lee et al., 2018). While the slope for this correlation (0.02) was small compared to those found with hemisWM or CSF, the measured variability of the ChPlex in our in-vivo cohort was by far the largest in any OFF region (0.85-7.25), allowing such a small slope to still produce significant variations in cortical SUVRs. However, the high uptake in the ChPlex affected the hippocampus but not the BA, so the spill-in from the ChPlex might be a minor issue when not including the hippocampus in BA I/II (Maass et al., 2017). Finally, negative correlations between the cerebWM and all cortical regions, as well as between the cerebWM and the CSF and the rest of OFF regions were observed in the simulations. Spill-in counts coming from the cerebWM (and the CSF) might artificially rise the uptake on the reference region (inferior cerebellar grey matter), thus reducing SUVRs for the rest of the regions. In general, the correlations described above (except the negative correlation with the cerebWM) disappeared after applying Baker's RBV on the simulated data, suggesting an excellent performance of this PVC, while

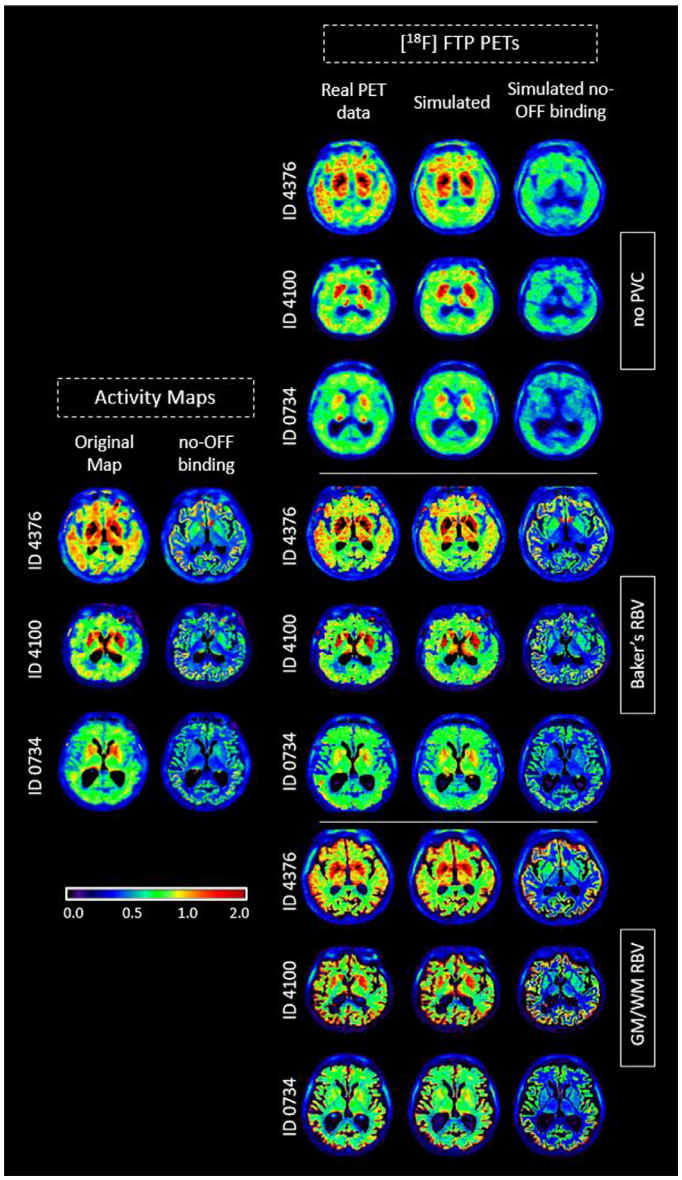

Fig. 3. Left: Examples of the simulated activity maps. Right: Comparison between real and simulated FTP PET images (including those corresponding to the no-OFF binding condition) for 3 of the 10 ADNI subjects before and after applying PVC (both Baker's and GM/WM RBV).

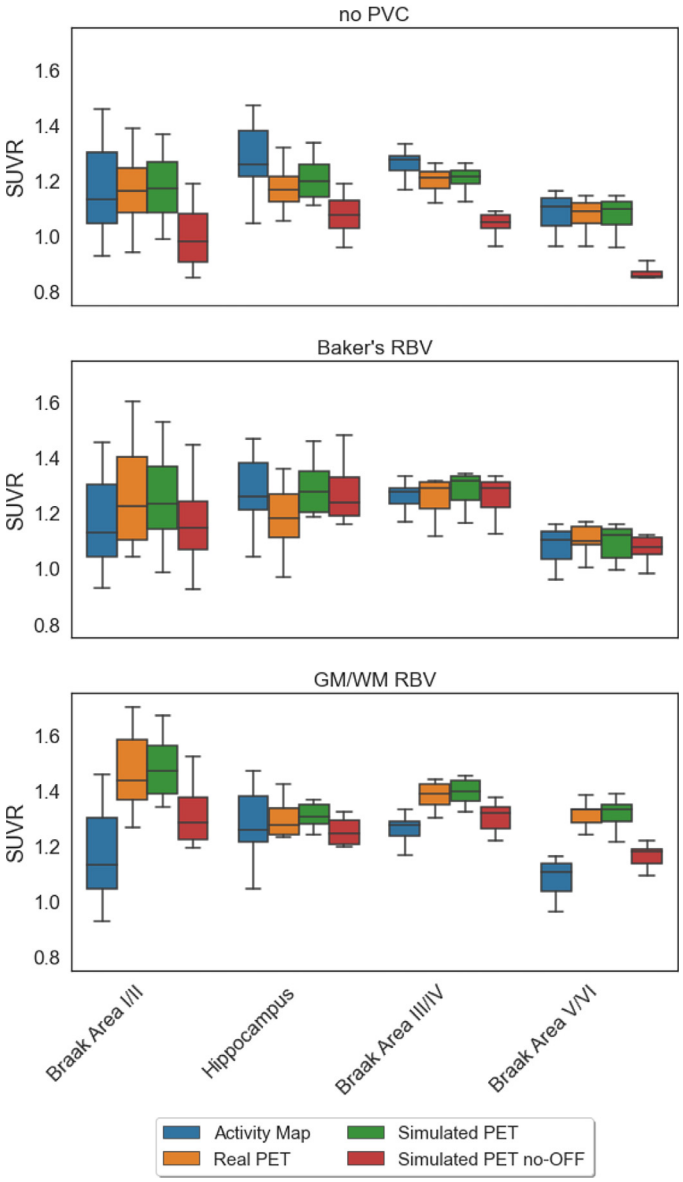

Fig. 4. SUVR comparison between real and simulated FTP PET images (including no-OFF binding results) for BA and hippocampus for non-PVC images (top panel), Baker's RBV PVE corrected images (middle panel) and GM/WM RBV PVE corrected images (bottom panel). The blue boxes represent the simulated SUVRs.

GM/WM RBV only reduced the correlations related with the hemisWM. As expected, Baker's RBV was superior to GM/WM RBV for the quantification of the hippocampus FTP SUVR due to the large contribution of the ChPlex. For most of the correlations observed on the simulations among these regions (hemisWM, CSF, ChPlex, cerebWM), we observed similar patterns in-vivo, but with higher slopes and PVC removing only a fraction of the effect (Fig. 5). In terms of the slopes of the observed correlations, we observed a reduction of around 0.2 after applying PVC in-vivo (≈50%), while these slopes were reduced to ~ 0 in the simulated data. These results seem to support previous hypotheses pointing that PVE is not the only contributor to these correlations on real subject data (Baker et al., 2019).

Our simulation experiments did not reveal any correlations between the rest of the OFF regions (caudate, putamen, pallidum and thalamus) or co-varying groups of OFF ROIs and cortical SUVRs. These correlations were found on in-vivo data but, while PVC (specially Baker's RBV) strongly reduced the variance for these correlations (Fig. 5), the slopes of the correlations were reduced only by 16.3% when applying Baker's RBV and even increased after GM/WM RBV, which contrasts with the reduction of about 50% with both PVCs for those ROIs where PVE was found to produce relevant spill-in on simulated data. These results might suggest that PVE is not the main contributor to the correlations between these OFF ROIs and BA in-vivo.

In summary, our results strongly suggest that the correlations between cortical and OFF regions are heavily influenced by factors other than PVE, as suggested by previous studies (Baker et al., 2019). On the one hand, the linear regression slopes were larger in-vivo than in simulated data, where PVE is the only correlation source (i.e., 0.63-0.67 vs 0.15-0.26 for the correlation between hemisWM and BA). On the other hand, the reduction of the slopes was notably higher in-vivo for those regions where significant PVE was observed in the simulations, pointing that PVE is not the main contributor to the correlations found with the remaining OFF regions. More suggestively, the reduction of

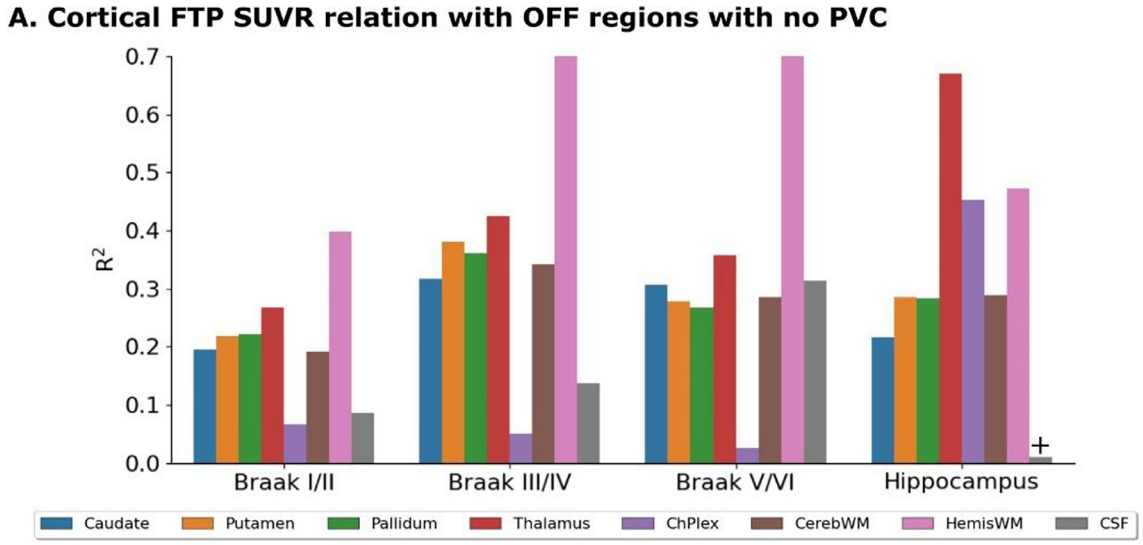

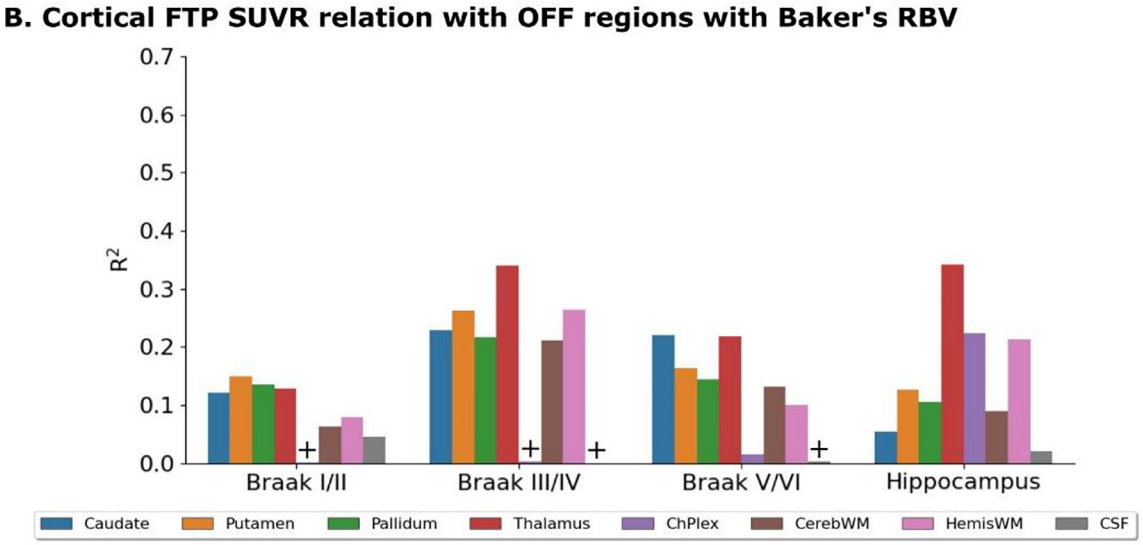

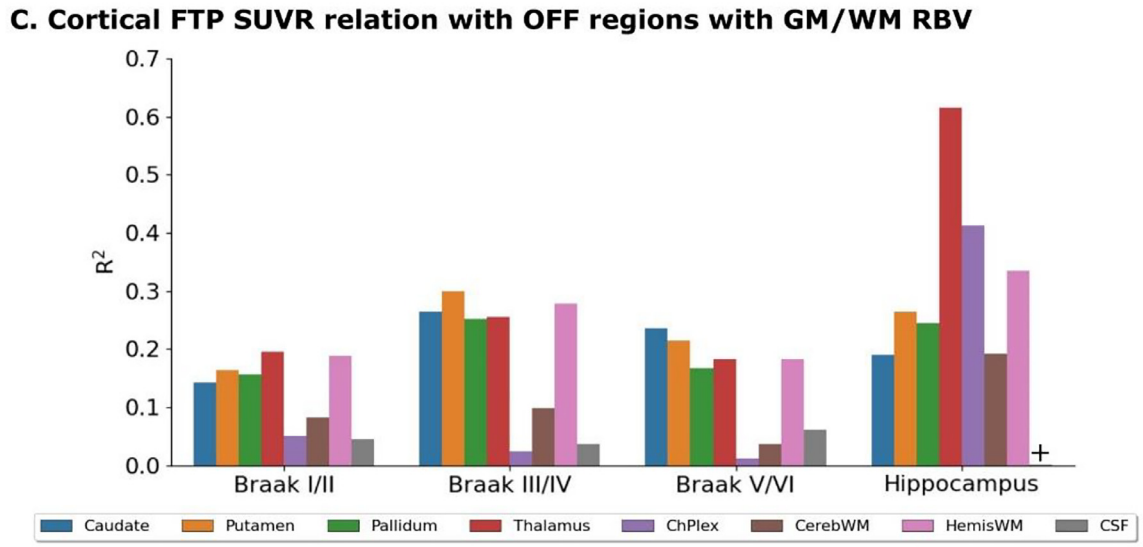

Fig. 5. R^2 values between OFF regions and quantified FTP SUVR values (+p>0.05). A) Before PVC. B) After Baker's RBV. C) After GM/WM RBV.

the slopes after PVC in-vivo was only slightly higher than the PVE contribution as measured by MC simulation (0.27-0.38 vs. 0.15-0.26 for the hemisWM). These results suggest that PVC might be effectively removing PVE in-vivo and that the remaining correlation is caused by non-PVE effects, such as underlying biological or tracer-related contributions (Baker et al., 2019).

Regarding the impact of PVC, despite not removing all correlations, it significantly improved the results of in-vivo quantification, so we still recommend applying PVC on FTP PET. Our simulation results suggest that Baker's RBV was able to remove almost all the PVE counts, while applying a simplified two-compartment mask removed all but the correlation between the ChPlex and the hippocampus. Yet, we would still recommend the Baker's approach for its much better representation of realistic SUVRs (Fig. 4) and more reliable behaviour overall (Table 4).

With regards to the limitations of this work, we point that our activity maps were extracted for only 10 subjects of the initial cohort of 309 $HC_{A\beta-}$, and all of them were scanned with the GE Discovery ST scanner. This choice was made in order to be able to use a previously validated MC model, available for this scanner, which achieves an excellent correspondence between simulated and real data (Paredes-Pacheco et al., 2021). While still present in many centers, the GE Discovery ST is a relatively old scanner, and we expect that PVEs will be smaller for modern scanners with better spatial resolutions. Furthermore, despite the excellent performance of our MC model, the use of modelling also comes with some inherent limitations. For example, we have used an adaptation of STIR for the reconstruction, but we assume that using the scanner reconstruction algorithm might produce more accurate results. Another limitation of this work is the absence of the skull and the meninges as OFF ROIs. Although OFF in these regions has been reported for second generation tau PET tracers such as [^{18}F]-MK-6240 and [^{18}F]RO948 (Betthauser et al., 2019; Smith et al., 2020) and demonstrated to produce spill-in effects into the cortex (Mertens et al., 2022), the segmentation of these regions based on T1 MRI data is challenging and these regions are not included in Baker's atlas (Baker et al., 2017). In addition, for correcting PVE, we used only one PVC technique (RBV) with two different masks. While differences are expected in performance when using other PVCs, we restricted to RBV as a standard PVC technique in the field. We expect that our GM/WM results would apply to other two-compartment PVCs. Finally, we performed our analysis only on $HC_{A\beta-}$. We expect the effect of PVE to be smaller in Aβ+ subjects, in whom a higher cortical FTP signal is expected.

5. Conclusions

The variability of cortical FTP SUVR is primarily influenced by PVE from the hemisWM and, to a lesser degree, by the CSF and the ChPlex. While the spill-out counts from the ChPlex have an impact on the hippocampus due to its proximity, the hemisWM and the CSF signal affects SUVR variability in all target regions. Although PVC improves image quantification, remaining correlations in vivo are not observed on a simulation environment, pointing to the existence of biological or tracer-related contributions to these correlations.

Declarations

Ethics approval and consent to participate

The ADNI studies were conducted according to Good Clinical Practice guidelines, US 21CFR Part 50– Protection of Human Subjects, and Part 56 – Institutional Review Boards (IRBs) / Research Ethics Boards (REBs), and pursuant to state and federal HIPAA regulations. Written informed consent for the study was obtained from all participants and/or authorized representatives.

Consent for publication

Not applicable

Availability of data and material

Patient data used in the preparation of this article were obtained from the Alzheimer's Disease Neuroimaging Initiative (ADNI) database. Data from the ADNI is open and can be obtained from the ADNI data repositories. The simulation datasets used for the present work are available for sharing from the corresponding author on reasonable request

Funding

This work is partly funded by the public projects funded by ERDF: PI16/01416 (ISCIII) and EAPA_791/2018 NeuroATLANTIC (UE Interreg). Francisco J. López-González and José Paredes-Pacheco are funded by PhD scholarships (FPU17/04470 and FPU16/05108, respectively) from the Spanish Ministry of Education, Culture and Sport under the FPU program. The project that gave rise to these results received the support of a fellowship from "la Caixa" Foundation (ID 100010434). The fellowship code is LCF/BQ/DR20/11790012. Pablo Aguiar is a Ramon y Cajal Fellow (RYC-2015/17430). Jesús Silva-Rodríguez is a Sara Borrell Fellow (CD21/00067).

Authors' contributions

JSR, AM and PA contributed to design of the study. FJLG and JPC performed the MC simulations. FJLG and ACS performed the data processing and analysis and drafted the original manuscript. JSR, PAF and AM contributed to the critical revision of the manuscript. All authors discussed the results and implications and commented on the manuscript. All authors read and approved the final manuscript.

Declaration of Competing Interest

JSR is an advisor for Qubiotech Health Intelligence SL. PAF is an advisor for Qubiotech Health Intelligence SL.

Credit authorship contribution statement

Francisco J. López-González: Data curation, Methodology, Investigation, Validation, Formal analysis, Writing – original draft, Visualization. **Alejandro Costoya-Sánchez:** Data curation, Methodology, Investigation, Validation, Formal analysis, Writing – original draft, Visualization. **José Paredes-Pacheco:** Investigation, Software, Writing – review & editing. **Alexis Moscoso:** Conceptualization, Writing – review & editing. **Jesús Silva-Rodríguez:** Conceptualization, Supervision, Project administration, Methodology, Validation, Writing – review & editing. **Pablo Aguiar:** Conceptualization, Supervision, Project administration, Resources, Funding acquisition, Writing – review & editing.

Acknowledgements

Data collection and sharing for this project was funded by the Alzheimer's Disease Neuroimaging Initiative (ADNI) (National Institutes of Health Grant U01 AG024904) and DOD ADNI (Department of Defense award number W81XWH-12-2-0012). ADNI is funded by the National Institute on Aging, the National Institute of Biomedical Imaging and Bioengineering, and through generous contributions from the following: AbbVie, Alzheimer's Association; Alzheimer's Drug Discovery Foundation; Araclon Biotech; BioClinica, Inc.; Biogen; Bristol-Myers Squibb Company; CereSpir, Inc.; Cogstate; Eisai Inc.; Elan Pharmaceuticals, Inc.; Eli Lilly and Company; EuroImmun; F. Hoffmann-La Roche

Ltd and its affiliated company Genentech, Inc.; Fujirebio; GE Healthcare; IXICO Ltd.; Janssen Alzheimer Immunotherapy Research & Development, LLC.; Johnson & Johnson Pharmaceutical Research & Development LLC.; Lumosity; Lundbeck; Merck & Co., Inc.; Meso Scale Diagnostics, LLC.; NeuroRx Research; Neurotrack Technologies; Novartis Pharmaceuticals Corporation; Pfizer Inc.; Piramal Imaging; Servier; Takeda Pharmaceutical Company; and Transition Therapeutics. The Canadian Institutes of Health Research is providing funds to support ADNI clinical sites in Canada. Private sector contributions are facilitated by the Foundation for the National Institutes of Health (www.fnih.org). The grantee organization is the Northern California Institute for Research and Education, and the study is coordinated by the Alzheimer's Therapeutic Research Institute at the University of Southern California. ADNI data are disseminated by the Laboratory for Neuro Imaging at the University of Southern California.

Supplementary materials

Supplementary material associated with this article can be found, in the online version, at doi:10.1016/j.neuroimage.2022.119396.

References

Akerele, M.I., Wadhwa, P., Silva-Rodriguez, J., Hallett, W., Tsoumpas, C., 2018. Validation of the physiological background correction method for the suppression of the spill-in effect near highly radioactive regions in positron emission tomography. EJNMMI Phys 5, 34. doi:10.1186/s40658-018-0233-8.

Aston, J.A.D., et al., 2002. Positron emission tomography partial volume correction: estimation and algorithms. J. Cereb. Blood Flow Metab. 22, 1019–1034. doi:10.1097/00004647-200208000-00014.

Baker, S.L., Harrison, T.M., Maass, A., La Joie, R., Jagust, W.J., 2019. Effect of Off-Target Binding on (18)F-Flortaucipir Variability in Healthy Controls Across the Life Span. J. Nucl. Med. 60, 1444–1451. doi:10.2967/jnumed.118.224113.

Baker, S.L., Maass, A., Jagust, W.J., 2017. Considerations and code for partial volume correcting [18F]-AV-1451 tau PET data. Data Br 15, 648–657. doi:10.1016/j.dib.2017.10.024.

Barret, O., et al., 2017. Kinetic Modeling of the Tau PET Tracer (18)F-AV-1451 in Human Healthy Volunteers and Alzheimer Disease Subjects. J. Nucl. Med. 58, 1124–1131. doi:10.2967/jnumed.116.182881.

Betthauser, T.J., et al., 2019. In Vivo Characterization and Quantification of Neurofibrillary Tau PET Radioligand ^{18}F-MK-6240 in Humans from Alzheimer Disease Dementia to Young Controls. J. Nucl. Med. 60, 93. doi:10.2967/jnumed.118.209650, LP–99.

Biel, D., et al., 2021. Tau-PET and in vivo Braak-staging as prognostic markers of future cognitive decline in cognitively normal to demented individuals. Alzheimers. Res. Ther. 13, 137. doi:10.1186/s13195-021-00880-x.

Braak, H., Braak, E., 1991. Neuropathological stageing of Alzheimer-related changes. Acta Neuropathol. 82, 239–259. doi:10.1007/BF00308809.

Chandra, A., et al., 2019. Applications of amyloid, tau, and neuroinflammation PET imaging to Alzheimer's disease and mild cognitive impairment. Hum. Brain Mapp. 40, 5424–5442. doi:10.1002/hbm.24782.

Chen, S.-D., et al., 2021. Staging tau pathology with tau PET in Alzheimer's disease: a longitudinal study. Transl. Psychiatry 11, 483. doi:10.1038/s41398-021-01602-5.

Chien, D.T. et al., 2013. Early Clinical PET Imaging Results with the Novel PHF-Tau Radioligand [F-18]-T807. J. Alzheimer's Dis. 34, 457–468. https://doi.org/10.3233/JAD-122059

Diedrichsen, J., Balsters, J.H., Flavell, J., Cussans, E., Ramnani, N., 2009. A probabilistic MR atlas of the human cerebellum. Neuroimage 46, 39–46. doi:10.1016/j.neuroimage.2009.01.045.

Gonzalez-Escamilla, G., Lange, C., Teipel, S., Buchert, R., Grothe, M.J., 2017. PETPVE12: an SPM toolbox for Partial Volume Effects correction in brain PET – Application to amyloid imaging with AV45-PET. Neuroimage 147, 669–677. doi:10.1016/j.neuroimage.2016.12.077.

Haynor, D.R., Harrison, R.L., Lewellen, T.K., 1991. The use of importance sampling techniques to improve the efficiency of photon tracking in emission tomography simulations. Med. Phys. 18, 990–1001. doi:10.1118/1.596615.

Hoffman, E.J., Huang, S.-C., Phelps, M.E., 1979. Quantitation in Positron Emission Computed Tomography: 1. Effect of Object Size. J. Comput. Assist. Tomogr. 3.

Hudson, H.M., Larkin, R.S., 1994. Accelerated image reconstruction using ordered subsets of projection data. IEEE Trans. Med. Imaging 13, 601–609. doi:10.1109/42.363108.

Johnson, K.A., et al., 2016. Tau positron emission tomographic imaging in aging and early Alzheimer disease. Ann. Neurol. 79, 110–119. doi:10.1002/ana.24546.

Klunk, W.E., et al., 2015. The Centiloid Project: standardizing quantitative amyloid plaque estimation by PET. Alzheimers. Dement. 11, 1–4. doi:10.1016/j.jalz.2014.07.003.

Lee, C.M., et al., 2018. 18F-Flortaucipir Binding in Choroid Plexus: Related to Race and Hippocampus Signal. J. Alzheimers. Dis. 62, 1691–1702. doi:10.3233/JAD-170840.

Leuzy, A., et al., 2019. Tau PET imaging in neurodegenerative tauopathies—still a challenge. Mol. Psychiatry 24, 1112–1134. doi:10.1038/s41380-018-0342-8.

Lowe, V.J., et al., 2016. An autoradiographic evaluation of AV-1451 Tau PET in dementia. Acta Neuropathol. Commun. 4, 58. doi:10.1186/s40478-016-0315-6.

Lu, Y. et al., 2021. Partial volume correction analysis for (11)C-UCB-J PET studies of Alzheimer's disease. Neuroimage 238, 118248. doi:10.1016/j.neuroimage.2021.118248.

Maass, A., et al., 2017. Comparison of multiple tau-PET measures as biomarkers in aging and Alzheimer's disease. Neuroimage 157, 448–463. doi:10.1016/j.neuroimage.2017.05.058.

Marti-Fuster, B., et al., 2014. Including anatomical and functional information in MC simulation of PET and SPECT brain studies. Brain-VISET: A voxel-based iterative method. IEEE Trans. Med. Imaging 33, 1931–1938. doi:10.1109/TMI.2014.2326041.

Mertens, N., et al., 2022. Impact of meningeal uptake and partial volume correction techniques on [18F]MK-6240 binding in aMCI patients and healthy controls. J. Cereb. Blood Flow Metab. 0271678X221076023. doi:10.1177/0271678X221076023.

Moscoso, A., Grothe, M.J., Schöll, M., 2021. Reduced [(18)F]flortaucipir retention in white matter hyperintensities compared to normal-appearing white matter. Eur. J. Nucl. Med. Mol. Imaging 48, 2283–2294. doi:10.1007/s00259-021-05195-5.

Nema, N.U., 2012. NU 2-2012: Performance Measurements of Positron Emission Tomographs. Rosslyn, VA Natl. Electr. Manuf. Assoc..

Ossenkoppele, R., et al., 2018. Discriminative Accuracy of [18F]flortaucipir Positron Emission Tomography for Alzheimer Disease vs Other Neurodegenerative Disorders. JAMA 320, 1151–1162. doi:10.1001/jama.2018.12917.

Paredes-Pacheco, J., et al., 2021. SimPET-An open online platform for the Monte Carlo simulation of realistic brain PET data. Validation for (18) F-FDG scans. Med. Phys. 48, 2482–2493. doi:10.1002/mp.14838.

Rousset, O.G., Ma, Y., Evans, A.C., 1998. Correction for Partial Volume Effects in PET: Principle and Validation. J. Nucl. Med. 39, 904 LP –911.

Roy, S., Banerjee, D., Chatterjee, I., Natarajan, D., Joy Mathew, C., 2021. The Role of 18F-Flortaucipir (AV-1451) in the Diagnosis of Neurodegenerative Disorders. Cureus 13, e16644. https://doi.org/10.7759/cureus.16644

Schöll, M., et al., 2016. PET Imaging of Tau Deposition in the Aging Human Brain. Neuron 89, 971–982. doi:10.1016/j.neuron.2016.01.028.

Schrouff, J., et al., 2013. PRoNTo: Pattern Recognition for Neuroimaging Toolbox. Neuroinformatics 11, 319–337. doi:10.1007/s12021-013-9178-1.

Schultz, S.A., et al., 2018. Widespread distribution of tauopathy in preclinical Alzheimer's disease. Neurobiol. Aging 72, 177–185. doi:10.1016/j.neurobiolaging.2018.08.022.

Schwarz, A.J., et al., 2018. Topographic staging of tau positron emission tomography images. Alzheimer's Dement. Diagnosis, Assess. Dis. Monit. 10, 221–231. doi:10.1016/j.dadm.2018.01.006.

Schwarz, A.J., et al., 2016. Regional profiles of the candidate tau PET ligand 18F-AV-1451 recapitulate key features of Braak histopathological stages. Brain 139, 1539–1550. doi:10.1093/brain/aww023.

Smith, R., et al., 2020. Head-to-head comparison of tau positron emission tomography tracers [18F]flortaucipir and [18F]RO948. Eur. J. Nucl. Med. Mol. Imaging 47, 342–354. doi:10.1007/s00259-019-04496-0.

Thielemans, K., et al., 2012. STIR: software for tomographic image reconstruction release 2. Phys. Med. Biol. 57, 867.

Thomas, B.A., et al., 2016. PETPVC: a toolbox for performing partial volume correction techniques in positron emission tomography. Phys. Med. Biol. 61, 7975–7993. doi:10.1088/0031-9155/61/22/7975.

Wang, L., et al., 2016. Evaluation of Tau Imaging in Staging Alzheimer Disease and Revealing Interactions Between β-Amyloid and Tauopathy. JAMA Neurol 73, 1070–1077. doi:10.1001/jamaneurol.2016.2078.

Wells, W.M., Viola, P., Atsumi, H., Nakajima, S., Kikinis, R., 1996. Multi-modal volume registration by maximization of mutual information. Med. Image Anal. 1, 35–51. doi:10.1016/S1361-8415(01)80004-9.

Wen, Q., et al., 2021. Tau-related white-matter alterations along spatially selective pathways. Neuroimage 226, 117560. doi:10.1016/j.neuroimage.2020.117560.

Xia, C.-F., et al., 2013. [(18)F]T807, a novel tau positron emission tomography imaging agent for Alzheimer's disease. Alzheimers. Dement. 9, 666–676. doi:10.1016/j.jalz.2012.11.008.

Yang, J., et al., 1996. Investigation of partial volume correction methods for brain FDG PET studies. IEEE Trans. Nucl. Sci. 43, 3322–3327. doi:10.1109/23.552745.